www.czasopisma.pan.pl PAN www.journals.pan.pl

Metrol. Meas. Syst., Vol. 23 (2016), No. 2, pp. 269–280.

METROLOGY AND MEASUREMENT SYSTEMS
Index 330930, ISSN 0860-8229
www.metrology.pg.gda.pl

IMPROVING SEGMENTATION OF 3D RETINA LAYERS BASED ON GRAPH THEORY APPROACH FOR LOW QUALITY OCT IMAGES

Agnieszka Stankiewicz1), Tomasz Marciniak1), Adam Dąbrowski1), Marcin Stopa2,3), Piotr Rakowicz2,3), Elżbieta Marciniak3)

1) Poznan University of Technology, Department of Computing, Piotrowo 3a, 60-965 Poznań, Poland
(agnieszka.stankiewicz@put.poznan.pl, ✉ tomasz.marciniak@put.poznan.pl, +48 61 647 5935, *adam.dabrowski@put.poznan.pl)*
2) Poznan University of Medical Sciences, Department of Optometry and Biology of Visual System, Rokietnicka 5D, 60-806 Poznań, Poland
3) Poznan University of Medical Sciences, Clinical Eye Unit and Pediatric Ophthalmology Service Heliodor Swiecicki University Hospital, Grunwaldzka 16/18, 60-780 Poznań, Poland (stopa@ump.edu.pl)

Abstract

This paper presents signal processing aspects for automatic segmentation of retinal layers of the human eye. The paper draws attention to the problems that occur during the computer image processing of images obtained with the use of the *Spectral Domain Optical Coherence Tomography* (SD OCT). Accuracy of the retinal layer segmentation for a set of typical 3D scans with a rather low quality was shown. Some possible ways to improve quality of the final results are pointed out. The experimental studies were performed using the so-called B-scans obtained with the OCT Copernicus HR device.

Keywords: Optical Coherence Tomography (OCT), segmentation of retinal layers, image segmentation, graph theory.

1. Introduction

In the contemporary ophthalmology, application of the computer-aided eye biometrics is an essential element that gives a possibility of lesion identification. Two techniques can be applied:

- ultrasound biometry, which uses ultrasonic waves to measure the distances between the structures of the eye (however, this technique requires a direct contact of the ultrasonic probe with the eye surface);
- optical biometry, which uses the *Optical Coherence Tomography* (OCT) technique and its advantage is the lack of the direct contact of hardware elements with the eyeball.

Many of advanced noninvasive measurement techniques use different kinds of light to examine the inner structure of a wide range of materials; among others there is the *Infrared* (IR) light, which is employed in the OCT [1, 2]. In the eye examination with the OCT, the device produces a light beam that is focused on the retina. The light, that is reflected from the internal structures of the eye, is analyzed with the means of interferometry by the device. The OCT images visualize the retinal layers.

An older, the so-called *Time Domain* (TD) OCT technology, uses a movable mirror and – for registration – a photodiode [3]. Contemporary OCT devices are based on the *Spectral Domain* (SD) analysis, in which the mirror is fixed and a spectrometer is used as the recorder.

The result of the OCT measurement with the use of these devices is a set of images of cross-sections (*i.e.* B-scans), which are constructed from a set of A-scans (amplitude modulation scans). A single B-scan image is noisy, thus in order to improve the image quality an averaging operation is applied, if we want to observe only a single image. For that purpose, several scans are gathered to create a single image ready for medical analysis. Such operation, though advantageous, considerably increases the acquisition time.

Article history: received on Sep. 30, 2015; accepted on Dec. 28, 2015; available online on May 16, 2016; DOI: 10.1515/mms-2016-0016.

In acquisition of a set of B-scans for a 3D image, the averaging operation is not applied. The data acquisition speed of typical OCT devices is 50 000 to 70 000 A-scans per second [4, 5], *i.e.*, if we want to get a 3D image composed of 100 B-Scans with the horizontal resolution of, say, 800 A-scans, the acquisition time is approximately 1.6 seconds. This time should not be extended to prevent artifacts associated with involuntary movements of the eyeball. Some manufacturers of the OCT devices use the technology of tracking the movement of the eyeball in order to prevent this problem.

The key element to effective operation of the diagnostic software is the correct determination of individual layers of the retina. Exact segmentation is an entry operation for the next stages of visualization. The following seven retina layers are typically analyzed: *Inner Limiting Membrane* (ILM), *Nerve Fiber Layer* (NFL) / *Ganglion Cell Layer* (GCL), *Inner Plexiform Layer* (IPL) / *Inner Nuclear Layer* (INL), INL / *Outer Plexiform Layer* (OPL), OPL / *Outer Nuclear Layer* (ONL), *Inner Segments* / *Outer Segments of Photoreceptors* (IS/OS), and *Retinal Pigment Epithelium* (RPE) / choroid. For example, the thickness of the retinal *Nerve Fiber Layer* (NFL) was frequently used during examination of glaucoma patients, while the measurements of the total retinal thickness (between NFL and RPE) were often used in assessment of patients with macular edema, choroidal neovascularization, and macular hole. An example of visible layers and their identification in a single OCT B-scan can be seen in Fig. 1.

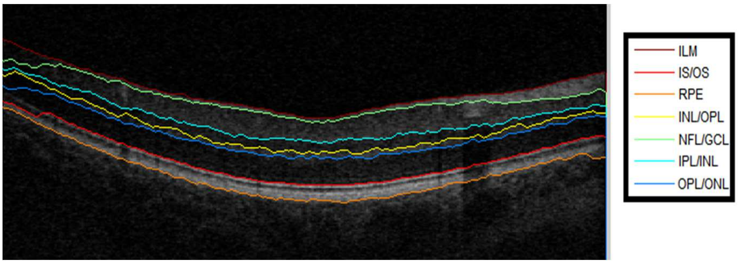

Fig. 1. An OCT image from a healthy patient with correctly segmented seven retinal boundaries: ILM, NFL/GCL, IPL/INL, INL/OPL, OPL/ONL, IS/OS, RPE.

The standard software of OCT devices includes algorithms for automatic segmentation of layers, which are *e.g.* based on: analysis of the image brightness [6], the technique of active contours [7], the pattern recognition [8], the graph theory [9–11], or techniques of grouping [12, 13]. Automatic layer segmentation of the retina in the OCT images requires overcoming many problems, such as noise [14], an uneven reflection of light by the tissues [15], absorption of light through the blood vessels, an unexpected movement of the patient, and the dependence of the proper segmentation algorithm on the device [16]. Particular difficulties are also introduced due to the presence of lesions [17]. All these aspects are considered in our analysis.

The B-scan quality can be assessed with the use of:

- the *Signal to Noise Ratio* (SNR);
- the *Signal Strength* (SS);
- the *Quality Index* (QI).

The first two indicators (SNR and SS) may be determined by the device manufacturer, whereas the QI is calculated from the image histogram and its value is close to the subjective evaluation carried out by the expert [18]. The QI is calculated by the device software in a standard way. Unfortunately, the respective formula is not provided by the device manufacturer. For example, in the case of a Copernicus HR OCT device, for a QI value below 4 it is advisable to repeat the examination, while for values above 6 the acquired set of images has a sufficient quality. For values between 4 and 6, the manufacturer suggests a careful analysis of the measurement results [4]. One should remember that for some lesions (*e.g.* cataract) a re-examination will not result in any improvement of the image quality. In addition, each OCT device may use a different scale of the image quality, making it difficult to compare scans obtained with various devices when using the indicators set by the manufacturers.

Figure 2 shows the B-scans obtained during the 3D OCT using the Copernicus HR device. The examination was made with the acquisition of 100 B-scans – each with a resolution of 800 pixels horizontally and 1,010 pixels vertically. An average QI determined by the manufacturer software was equal to 4.52.

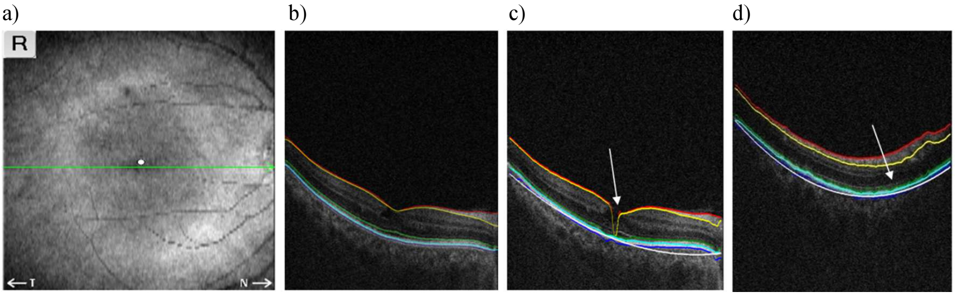

Fig. 2. Sample 3D OCT examination – 100×800×1010 data points: a) fundus reconstruction; b) B-scan No. 53 with expert's assignments, QI = 5.29; c) B-scan No. 52 with automatic assignments, QI = 5.29; d) B-scan No. 8 with automatic assignments, QI = 2.01; places with erroneous segmentation are indicated with arrows.

We see that the B-scan in Fig. 2c has a good quality, *i.e.* QI = 5.29, but even then the lesions can cause errors in the segmentation, with respect to manual determinations made by the human expert (Fig. 2b). A similar situation also occurs for the scan in Fig. 2d, which does not include a lesion, but its low quality caused by the acquisition also results in problems with the correct segmentation of layers.

2. Segmentation of Retina Layers in OCT images

As mentioned above, designation of the retina morphological structure (through analysis of retinal layers) is essential for the eye disease diagnosis. The presented experiment was designed to examine the effect of the OCT image quality on correctness of automatic segmentation of retina layers. For this purpose, a very efficient algorithm for image segmentation based on the graph theory was applied [10]. This was followed by removing portions of the image with low signal levels to improve the segmentation effectiveness. The results of the experiment are presented in section 4.

2.1. Segmentation algorithms based on graph theory

The applied algorithm is based on the use of a single OCT B-scan image *f* of the size $M \times N$ pixels as a graph *G*, in which each pixel $p \in P$ is treated as a node $v \in V$ of the graph connected with other nodes by edges $e \in \mathcal{E}$. A selection of connections between the nodes creates a path between the start and end nodes of the graph. Given a set of K non-intersecting layers $\{l_1(i), l_2(i), \ldots, l_K(i)\}$ that divide the graph into $K+1$ regions, the final path defining each layer is dependent on the nonnegative weights (costs) $w_k(e)$ assigned to the edges of the graph. The cost of the cut is defined by the sum of weights for the path (1):

$$C_{l_k(i)} = \sum_{\{(i,j)|j=l_k(i)\}} w_k(i,j) \qquad k \in \langle 1, K \rangle . \tag{1}$$

The algorithm is aimed at selection of a path that has the lowest total sum of weights (using the Dijkstra algorithm [19]). This path designates the border between neighboring layers of the retina that can be defined as a transition between two different brightness regions, as can be seen in Fig. 3.

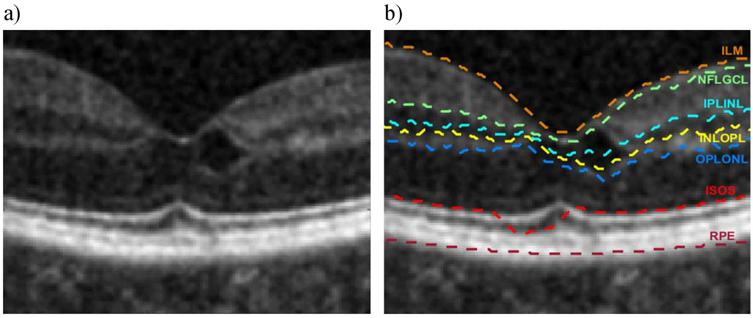

Fig. 3. An illustration of layers to be segmented on the macular OCT cross-section: a) center of the B-scan image and b) assignments of the seven segmented layers.

The key element in this method is the right assignment of weights to the edges of the graph. In the literature, various methods for computing the weights are mentioned [20]. They use a function of the distance between pixels or the difference of their brightness. Since most features of interest have a smooth transition between neighboring pixels, due to a relatively high resolution of the SD-OCT retinal scans, each node is associated with only its eight nearest neighbors. Thanks to that, there is no need to incorporate geometric distance weights. All other node pairs are disconnected, resulting in a sparse adjacency matrix of intensity difference graph weights. We then define the graph to be undirected, thus halving the size of the adjacency matrix. The applied solution enables to assign low weight values to the edges of the searched object (the border of the retina layer) in opposition to the rest of the image. This is based on the assumption that the segmented object has the features distinguishing it from the surrounding area. This is possible due to the fact that the neighboring layers of the retina have different reflectivities, thus causing differences in brightness between pixels of the image in the vertical direction (see Fig. 3). This enables to calculate the weights (2) using the vertical gradient values [10]:

$$w_k(a,b) = 2 - \left(\frac{\partial f(a)}{\partial y} + \frac{\partial f(b)}{\partial y} \right) + w_{\min}, \tag{2}$$

where $w_k(a,b)$ represents the weight of the graph edge between nodes a and b, the brightness gradients $\partial f / \partial y$ for the nodes a and b are normalized to values between 0 and 1, while w_{min} is the minimal weight of the graph (set at a low positive value equal to 10^{-5}) that enables to maintain the system stability. From (2), we can see that low weight values are assigned to the node pairs with large vertical gradients. In this way, the calculated weights are gathered in the adjacency matrix, whose elements represent costs of crossing the graph nodes. It should also be mentioned that this solution yields two undirected adjacency matrixes designed for dark-to-light and light-to-dark intensity transitions.

In the proposed algorithm, the start and end nodes of the graph are predefined as the top left and the bottom right corners of the image, in contrast to methods that calculate the shortest path between every possible pair of nodes in the graph.

In the next step, an empty column (with zero crossing weights) is added at each side of the image. This initialization is based on the assumption that the segmented layers extend to the entire width of the analyzed image.

In the final step, the added columns can be deleted, thus returning to the original image with the obtained segmentation. An illustrative B-scan image segmentation using this automatic method is presented in Fig. 4. The red dashed line illustrates the cut made with the Dijkstra algorithm.

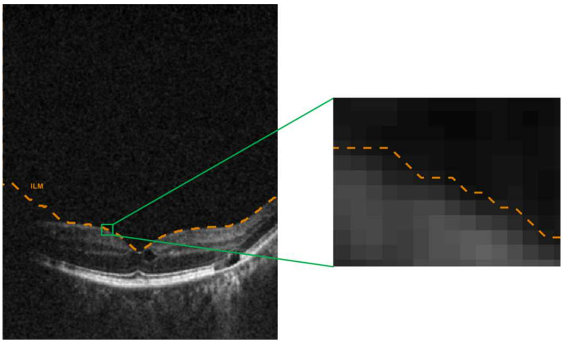

Fig. 4. An example of the OCT image segmentation method.

Considering the presence of layers with similar characteristics (*e.g.* brightness, density) in a close proximity to each other, it is desirable to limit the search area for each layer. This means that before finding the shortest path the edges that are outside the desired region of interest are removed from the graph . In practice, defining these regions is not an easy task and may require prior knowledge of the structure of the tissues presented in the image.

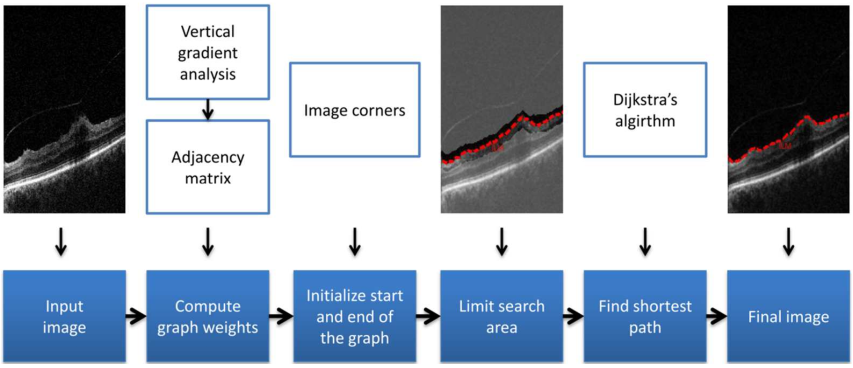

Fig. 5. A general scheme of the ILM retina layer segmentation of the OCT B-scan.

Given the information that the retinal layers are by the definition continuous in the plane of a single image as well as between the cross-sections, the algorithm was expanded to limit the search region of the graph for two of the most prominent layers based on their location in the neighboring cross-sections (images).

A general scheme visualizing the algorithm presented above is shown in Fig. 5.

2.2. Adaptive method of removing low quality signal

The detailed analysis of the OCT B-scan images shows that there exist regions with a very low signal, causing retinal layers to be almost entirely invisible near the lateral edges of the scan. This phenomenon occurs due to underexposure of the tissues in the periphery of the scan. An illustrative cross-section with this type of defect and the reconstructed corresponding fundus image are presented in Fig. 6. Since such a situation is in conflict with the assumption of the continuity of the layers through the entire image, it is the main cause of errors during the automatic image segmentation. The segmentation error is defined as the difference between the automatic and manual assignments of the layers for each column of the image.

The performed research includes removal of some parts of the B-scan image along sides in order to overcome the discussed obstacle. The best method to define the area to be removed is to apply adaptive techniques. The point at which a single B-scan image (of size M by N) should be cropped is defined by finding the first side column i, in which the maximum value of the brightness X is higher than the predefined threshold t, as it is described by (3):

$$i : \max_{j \in <1,M>} (X_{ij}) < t \qquad i \in \langle 1, N \rangle \ . \tag{3}$$

Despite its higher computational requirements and time consumption, the adaptive method enables to obtain better results than easier and faster methods of removing parts of the image with a constant width.

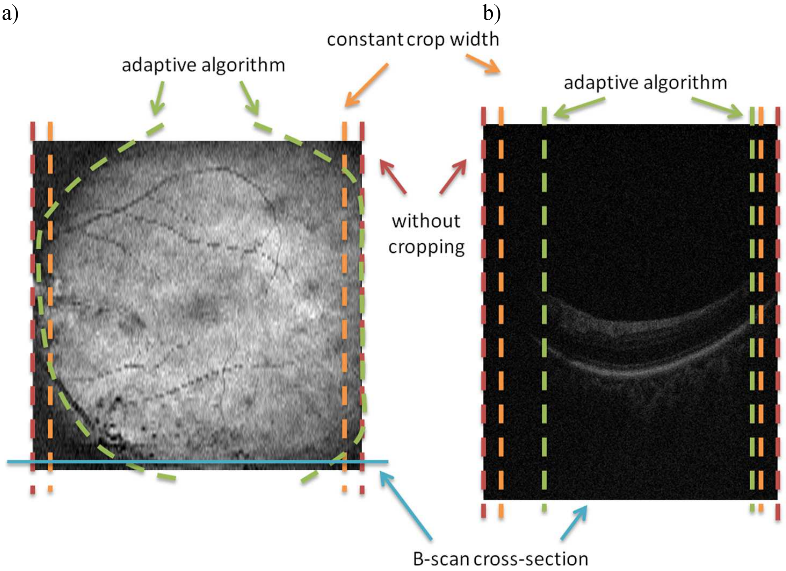

Fig. 6. An illustration of three examined methods of reducing the impact of a low level signal area on the correctness of automatic segmentation algorithm in an example of: a) the reconstructed fundus image; b) the B-scan image.

Figure 6 presents the applied methods of removing low quality parts of an image. The dashed lines represent examples of cut lines: the red line – the initial image without cutting, the orange line – the image cut with a constant width, the green line – the image cut with an adaptively computed width. In Section 4 there are presented the results of the performed experiments comparing their accuracy for the proposed method of removing low quality parts of the scan.

Metrol. Meas. Syst., Vol. 23 (2016), No. 2, pp. 269–280.

3. Data and implementation

To test the accuracy of the proposed method, we used a series of 3D OCT scans gathered with the Copernicus HR (OPTOPOL Technology Sp. z o.o., Zawiercie, Poland) device. The scans of the retina were collected from 30 patients with symptoms of vitreoretinal interface pathologies. The average age of the examined patients was 70 years. For each patient an 8 mm × 8 mm × 2 mm macular scan was performed with the volume of 100 × 800 × 1010 points (100 B-scan images with the resolution of 800 × 1010 pixels).

The methodology of the experiments included manual assignment of the correct segmentation of seven retina layers and its comparison with the automatic segmentations that were obtained using the presented graph theory approach. The layers were selected and manually assigned by the experts from the Clinical Eye Unit, Heliodor Święcicki University Hospital, Poznan University of Medical Sciences, Poland. The accuracy assessment involved calculation of the arithmetic average of the absolute error in pixels (4) as well as its standard deviation (5), while the error was defined as the difference between the manual and automatic assignments:

$$\mathrm{ME}_k = \frac{1}{N}\sum_{i=1}^{N}\left|L_k(i) - \hat{L}_k(i)\right| \qquad k \in \langle 1,7 \rangle, \tag{4}$$

$$\sigma_k = \sqrt{\frac{1}{N}\sum_{i=1}^{N}\left(\left|L_k(i) - \hat{L}_k(i)\right| - \mathrm{ME}_k\right)^2}, \tag{5}$$

where $L_k(i)$ and $\hat{L}_k(i)$ represent the values of layer k segmented in the manual and automatic ways, respectively, ME_k is the arithmetic average of the error for layer k, and N stands for the number of pixels, for which both manual and automatic assignments exist. It is worth mentioning that due to a dissimilarity, in which the borders between layers are found by the human expert and by the algorithm, the difference between the assignments that is less than 5 pixels is treated as the exact 0 error value. The algorithm was implemented in the Matlab/Simulink environment.

4. Comparison of standard segmentation method and adaptive improvement technique

In this section the results of the proposed algorithm for automatic segmentation of seven retina layers are presented. A set of 15 scans (15 eyes) from 12 patients was selected for this experiment. The average value of the QI parameter calculated for these scans by the OPTOPOL SOCT software is 4.17, thus their quality can be classified as low.

The performed experiment was aimed at testing two of the proposed methods for improving accuracy of the automatic image analysis:

- additional tracking of surfaces of ILM and IS/OS borders, and
- a method for removing low quality lateral parts of an image based on adaptive and constant (10% in both sides) image width cropping.

The results of the experiments are presented in Fig. 7 and Tables 1–3. Their analysis leads to the conclusion that both tracking of layers (limitation of the searched region of interest) and removal of low quality signal parts of the image can significantly improve the algorithm efficiency.

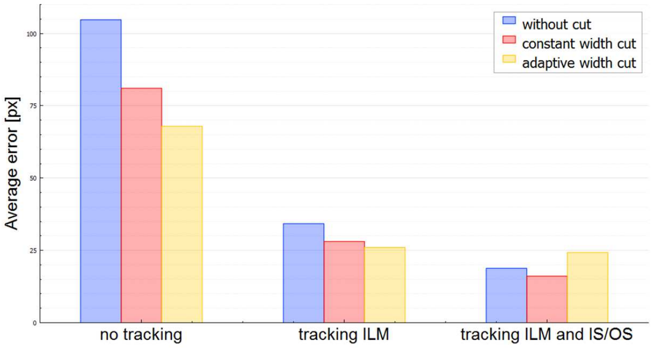

Fig. 7. An average error graph for each of the automatic segmentation methods.

Table 1. The average absolute error values and the standard deviations of the automatic retinal layer segmentation algorithm without cutting areas of low signal levels.

	Base algorithm			Additional tracking of ILM layer			Additional tracking of ILM and IS/OS layers		
layer	average error [px]	standard deviation [px]	percentage of erroneous segmentation	average error [px]	standard deviation [px]	percentage of erroneous segmentation	average error [px]	standard deviation [px]	percentage of erroneous segmentation
average value	**104.71**	**167.88**	**65.68%**	**34.23**	**83.49**	**44.57%**	**18.81**	**43.04**	**39.12%**
ILM	203.90	254.95	57.56%	17.58	44.13	21.63%	16.47	42.82	20.23%
NFL/GCL	169.79	212.29	75.14%	31.78	48.92	46.78%	20.88	36.80	41.21%
ONL/INL	129.26	156.10	82.96%	54.78	95.56	58.17%	28.17	53.11	52.98%
INL/OPL	112.40	136.91	81.94%	23.44	27.54	56.86%	21.85	27.07	51.54%
OPL/ONL	84.49	105.95	79.40%	80.71	164.60	52.58%	28.89	70.27	45.41%
IS/OS	15.26	36.60	48.31%	15.08	36.38	44.85%	7.97	18.79	34.49%
RPE/ Choroid	17.79	38.27	34.44%	14.19	38.90	31.08%	7.36	20.92	27.98%

Table 2. The average absolute error values, the standard deviations, and the percentages of erroneous segmentation for the automatic retinal layer segmentation algorithm using the truncated B-scan image of a constant width value (2 × 40 pixels = 10% image width).

	Base algorithm			Additional tracking of ILM layer			Additional tracking of ILM and IS/OS layers		
layer	average error [px]	standard deviation [px]	percentage of erroneous segmentation	average error [px]	standard deviation [px]	percentage of erroneous segmentation	average error [px]	standard deviation [px]	percentage of erroneous segmentation
average value	**81.04**	**151.54**	**52.61%**	**28.08**	**74.25**	**38.30%**	**16.09**	**39.41**	**31.25%**
ILM	155.30	238.35	42.49%	13.67	40.32	15.29%	13.31	39.85	13.44%
NFL/GCL	131.39	198.84	59.50%	26.17	44.03	38.60%	17.42	32.93	32.14 %
ONL/INL	99.83	143.04	67.76%	44.89	84.89	50.67%	23.71	45.23	44.23 %
INL/OPL	86.48	122.98	66.72%	20.83	25.58	49.62%	19.64	25.10	42.70 %
OPL/ONL	65.03	93.86	63.63%	66.07	148.08	45.63%	25.48	67.81	36.79 %
IS/OS	12.55	32.19	41.71%	12.59	32.19	39.28%	6.70	15.00	27.97 %
RPE/ Choroid	15.47	35.09	26.45%	10.96	32.73	29.03 %	6.26	17.55	21.44 %

Table 3. The average absolute error values, the standard deviations, and the percentages of erroneous segmentation for the automatic retinal layer segmentation algorithm using the truncated B-scan image of a width calculated on the basis of the signal quality level.

	Base algorithm			**Additional tracking of ILM layer**			**Additional tracking of ILM and IS/OS layers**		
layer	average error [px]	standard deviation [px]	percentage of erroneous segmentation	average error [px]	standard deviation [px]	percentage of erroneous segmentation	average error [px]	standard deviation [px]	percentage of erroneous segmentation
average value	**67.90**	**140.47**	**46.30%**	**26.03**	**61.33**	**31.84%**	**24.26**	**57.81**	**24.81%**
ILM	126.42	224.55	37.19%	32.89	67.70	6.87%	32.36	67.44	6.87%
NFL/GCL	107.96	184.36	53.11%	32.48	55.55	32.82%	32.01	55.09	24.92%
ONL/INL	84.66	135.63	62.90%	36.24	69.46	44.58%	34.71	66.71	37.64%
INL/OPL	75.22	117.93	61.67%	21.34	31.84	42.54%	20.61	30.50	35.61%
OPL/ONL	56.22	88.80	59.00%	38.45	100.43	38.13%	35.11	91.94	29.78%
IS/OS	11.56	28.02	33.59%	9.31	27.45	34.55%	6.44	18.81	23.61%
RPE/ Choroid	12.28	31.47	16.63%	10.62	29.87	23.43%	7.64	21.25	15.23%

In the case of additional tracking of ILM and IS/OS borders, almost twice as much pixels is erroneously segmented, while the average error is 5 times smaller. On the other hand, exclusion of low quality signal parts leads to a smaller segmentation error value for all layers. Despite the fact, that for the best combination of methods, even almost ¼ of pixels is erroneously segmented, they are assigned very near the manual segmentation borders, which is proved by the average error value of 16.1 pixels. This means a high efficiency of the proposed approach. High values of the standard deviation occur due to high error values of the segmentation process in the peripheral regions of cross-sections with very low QI (*i.e.*, below 2).

The performed segmentation of layers enables to generate a virtual profile map of the distances between the selected layers, as proposed in [21]. Such a detailed analysis is used by the specialists of ophthalmology to estimate abnormalities in the retinal structure. Fig. 8 presents an illustrative virtual map between ILM and IS/OS borders for the manual (a) and automatic (b, c, d) assignments. The circular ETDRS grid (with the circle diameters of 1, 3 and 6 mm) was placed on the image as the reference grid for medical purposes.

A close analysis of the generated maps shows that exclusion of low quality parts visually improves the algorithm accuracy. Fig. 8b demonstrates artifacts in the peripheral sections of the scan as well as errors in segmentation between the 90th and 100th cross-sections. Elimination of the selected parts improves the segmentation as it is seen in Fig. 8c and 8d.

5. Conclusion

The performed experiments prove that the accurate analysis of low quality OCT images is possible even when standard methods provided by the manufacturer are no longer viable (as shown in Fig. 2). Additionally, the graph-based method of 3D data segmentation proves to be one of the fastest and most accurate solutions. However, in cases of underexposure or the presence of lesions, this algorithm needs a further adjustment.

The proposed adaptive solution improves accuracy of the segmentation that is the first and crucial step for further calculations in the process of medical diagnosis. In the case of 3D OCT scans, the analysis of layers is performed with higher precision if each B-scan image is analyzed individually but with taking the neighboring images into account.

The proposed technique guarantees a precision that is necessary for generation of virtual maps of the distances between the selected retinal layers. These virtual maps support tracking the disease progression and selecting an appropriate treatment strategy, both pharmacological and surgical, as proved in article [21]. Moreover, the precise virtual maps help in selection of the best positioning of surgical tools during the vitrectomy surgery.

Further work will aim at combining several 3D OCT data matrices obtained with various resolution parameters to maximize the informative content of data between the subsequent cross-sections.

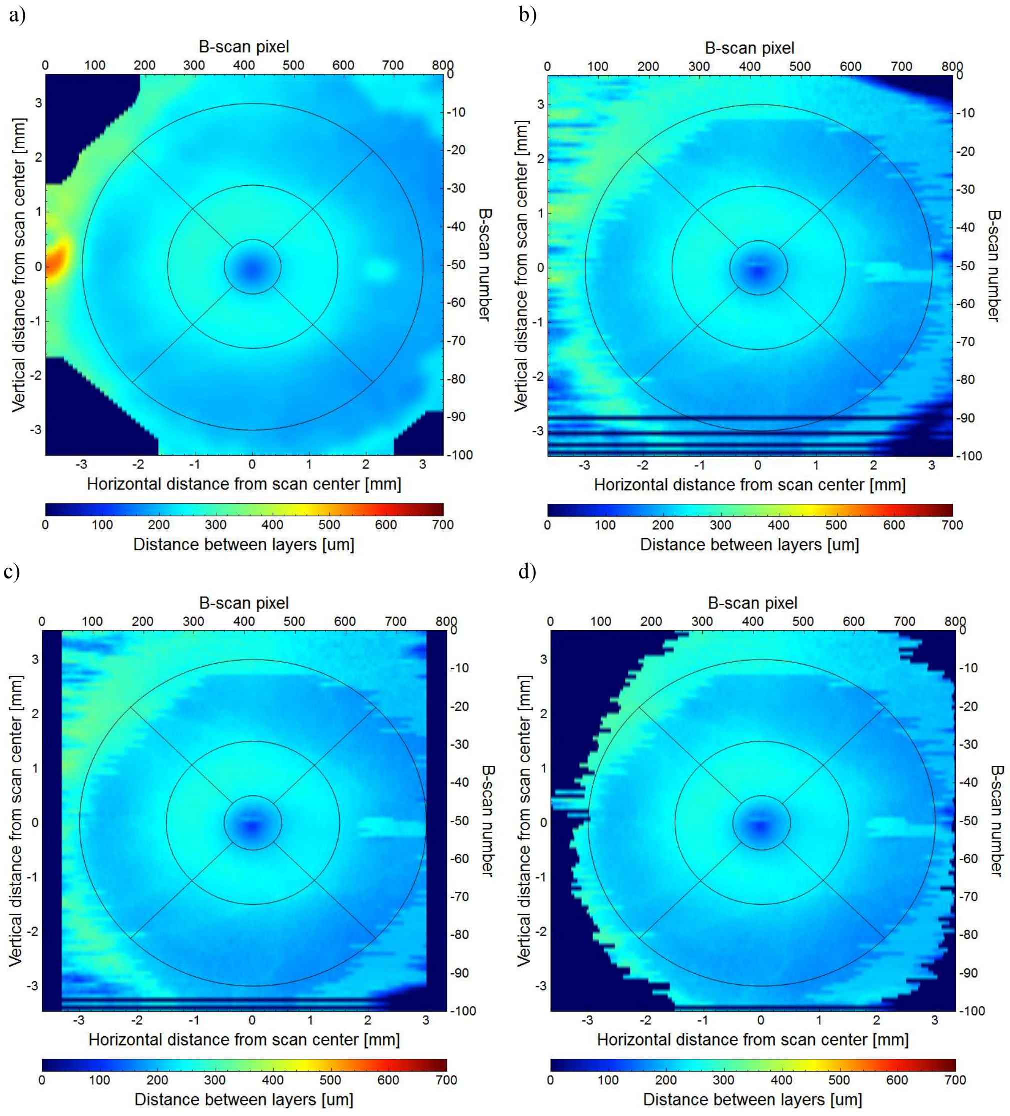

Fig. 8. The virtual maps between ILM and IS/OS segmented layers for: a) manual, and automated segmentations carried out; b) without cutting areas of low signal level; c) with cropping the B-scan image with a selected constant width; d) with the adaptive technique of removing the low quality area.

Acknowledgments

This work was prepared within the PRELUDIUM CADOCT-Project (09/93/PNCN/0710) founded by National Science Centre Poland.

References

[1] Rogalski, A., Chrzanowski, K. (2014). Infrared Devices And Techniques (Revision). *Metrol. Meas. Syst.*, 21(4), 565–618.

[2] Antoniuk, P., Strąkowski, M.R., Pluciński, J., Kosmowski, B.B. (2012). Non-Destructive Inspection Of Anti-Corrosion Protective Coatings Using Optical Coherent Tomography. *Metrol. Meas. Syst.*, 19(2), 365–372.

[3] Yaqoob, Z., Wu, J., Yang, C. (2005). Spectral domain optical coherence tomography: a better OCT imaging strategy. *Biotechniques*, 39 (6 Suppl), 6–13, DOI: 10.2144/000112090.

[4] SOCT Copernicus HR. (2011). User Manual Software Version 4.3.0 User Manual rev. A. *Optopol.*

[5] RTVue XR 100 Avanti Edition (2014). Podręcznik użytkownika. *Optovue Inc.*

[6] Fabritius, T., Makita, S., *et al.* (2009). Automated segmentation of the macula by optical coherence tomography. *Opt. Express*, 17(18), 15659–15669.

[7] Yazdanpanah, A., Hamarneh, G., Smith, B., Sarunic, M. (2009). Intra-retinal Layer Segmentation in Optical Coherence Tomography Using an Active Contour Approach. *Proc. of the 12th International Conference on Medical Image Computing and Computer-Assisted Intervention: Part II*, Springer-Verlag, 5762, 649–656.

[8] Kajic, V., Povazay, B., Hermann, B., Hofer, B., Marshall, D., Rosin, P.L., Drexler, W. (2010). Robust segmentation of intraretinal layers in the normal human fovea using a novel statistical model based on texture and shape analysis. *Optics Express*, 18(14), 14730–14744.

[9] Garvin, M.K., Abramoff, M.D., Kardon, R., Russell, S.R., Wu, X., Sonka, M. (2008). Intraretinal Layer Segmentation of Macular Optical Coherence Tomography Images Using Optimal 3-D Graph Search. *IEEE Transactions on Medical Imaging*, 27(10), 1495–1505.

[10] Chiu, S.J., Li, X.T., Nicholas, P., Toth, C.A., Izatt, J.A., Farsiu, S. (2010). Automatic segmentation of seven retinal layers in SDOCT images congruent with expert manual segmentation. *Opt. Express*, 18(18), 19413–19428.

[11] Teng, P. (2013). Caserel – An Open Source Software for Computer-aided Segmentation of Retinal Layers in Optical Coherence Tomography Images. *Zenodo*, DOI: 10.5281/zenodo.17893.

[12] Cha, Y.M., Han, J.H. (2014). High-Accuracy Retinal Layer Segmentation for Optical Coherence Tomography Using Tracking Kernels Based on Gaussian Mixture Model. *IEEE Journal of Selected Topics in Quantum Electronics*, 20(2).

[13] Szkulmowski, M., Wojtkowski, M., Sikorski, B., Bajraszewski, T., Srinivasan, V.J., Szkulmowska, A., Kaluzny, J.J., Fujimoto, J.G., Kowalczyk, A. (2007). Analysis of posterior retinal layers in spectral optical coherence tomography images of the normal retina and retinal pathologies. *Journal of Biomedical Optics*, 12(4).

[14] Szkulmowski, M., Wojtkowski, M. (2013). Averaging techniques for OCT imaging. *OPTICS EXPRESS*, 21(8), 9757–9773.

[15] Ishikawa, H., Stein, D.M., *et al.* (2005). Macular segmentation with optical coherence tomography. *Invest. Ophthalmol. Vis. Sci.*, 46(6), 2012–2017.

[16] Ehnes, A., Wenner, Y., Friedburg, C., Preising, M.N., Bowl, W., Sekundo, W., Meyer zu Bexten, E., Stieger, K., Lorenz, B. (2014). Optical Coherence Tomography (OCT) Device Independent Intraretinal Layer Segmentation. *Trans. Vis. Sci. Tech.*, 3(1).

[17] Fernández, D.C., *et al.* (2005). Automated detection of retinal layer structures on optical coherence tomography images. *Opt. Express*, 13(25), 10200–10216.

[18] Stein, D. M., *et al.* (2015). A New Quality Assessment Parameter for Optical Coherence Tomography. *The British Journal of Ophthalmology*, 90.2, 186–190.

[19] Dijkstra, E.W. (1959). A note on two problems in connexion with graphs. *Numerische Mathematik*, 1(1), 269–271.

[20] Shi, J., Malik, J. (2000). Normalized Cuts and Image Segmentation. *IEEE Trans. Pattern Anal. Mach. Intell.*, 22(8), 888–905.

[21] Stankiewicz, A., Marciniak, T., Dąbrowski, A., Stopa, M., Marciniak, E. (2014). A New OCT-based Method to Generate Virtual Maps of Vitreomacular Interface Pathologies. *Proc. of SPA 2014: Signal Processing Algorithms, Architectures, Arrangements, and Applications Conference*, 83–88.